INCREASED MACH NUMBER CAPABILITY FOR THE NASA GLENN 10X10 SUPERSONIC WIND TUNNEL

J. W. Slater and J. D. Saunders
NASA John H. Glenn Research Center
Cleveland, Ohio

ABSTRACT

Computational simulations and wind tunnel testing were conducted to explore the operation of the Abe Silverstein Supersonic Wind Tunnel at the NASA Glenn Research Center at test section Mach numbers above the current limit of Mach 3.5. An increased Mach number would enhance the capability for testing of supersonic and hypersonic propulsion systems. The focus of the explorations was on understanding the flow within the second throat of the tunnel, which is downstream of the test section and is where the supersonic flow decelerates to subsonic flow. Methods of computational fluid dynamics (CFD) were applied to provide details of the shock / boundary layer structure and to estimate losses in total pressure. The CFD simulations indicated that the tunnel could be operated up to Mach 4.0 if the minimum width of the second throat was made smaller than that used for previous operation of the tunnel. Wind tunnel testing was able to confirm such operation of the tunnel at Mach 3.6 and 3.7 before a hydraulic failure caused a stop to the testing. CFD simulations performed after the wind tunnel testing showed good agreement with test data consisting of static pressures along the ceiling of the second throat. The CFD analyses showed increased shockwave / boundary layer interactions, which was also observed as increased unsteadiness of dynamic pressures collected in the wind tunnel testing.

NOMENCLATURE

0	Flow station at the exit of the bellmouth ahead of the flexible-wall nozzle
1	Flow station downstream of the second throat and upstream of Turn 1
CFD	Computational Fluid Dynamics
p	Static pressure
p_t	Total pressure
Re	Reynolds number
SWT	Supersonic Wind Tunnel
TPR	Tunnel Pressure Ratio (p_{t0} / p_{t1})
T	Static temperature
T_t	Total temperature
w_{th}	Width of the second throat at its minimum area
x	Coordinate for the axial station along the second throat
y^+	Non-dimensional distance to the wall in the normal direction

INTRODUCTION

The Abe Silverstein Supersonic Wind Tunnel is located at the NASA John H. Glenn Research Center in Cleveland, Ohio[1]. It is commonly referred to as the 10x10 supersonic wind tunnel (10x10 SWT) since the cross-section of its test section is 10-foot by 10-foot. The tunnel was designed to operate up to Mach 4.0 in the test section; however, operational factors have limited the speeds to Mach 3.5. Above Mach 3.5, the tunnel has exhibited instabilities within the second throat. The second throat is a feature of some supersonic wind tunnels and consists of a decrease in flow area downstream of the test section which decelerates the supersonic flow to subsonic conditions through a system of shock waves with subsequent loss in total pressure[2]. If the shock system in the second throat moves upstream through the test section, the flow in the test section undergoes a violent change as the supersonic flow becomes unsteady and subsonic. This phenomenon is termed “tunnel unstart”. Unstart events can cause damage to models in the test section by imposing excessive loads onto the model.

A number of studies over the years have explored modifying the second throat or changing the manner in which the second throat is operated to allow operation of the 10x10 SWT up to Mach 4.0 without the instabilities and potential for tunnel unstart. An increased Mach number would be of interest because it would enhance the capability for testing of supersonic and hypersonic propulsion systems.

The current paper discusses the latest study for increasing the speed within the 10x10 SWT test section to Mach 4.0. The focus of the study was on understanding the stability and performance limits of the shock system in the second throat. The flow within the second throat was considered analogous to that in the throat of a mixed-compression inlet containing an isolator where a shock train of oblique and normal shocks interact with turbulent wall boundary layers to decelerate supersonic flow to subsonic flow in a diverging duct. The study involved both computational simulations and wind tunnel testing. The 10x10 SWT is described within this paper to identify key features of the tunnel, establish the limits of the compressors, and describe the operation of the second throat.

Methods of computational fluid dynamics (CFD) were applied to simulate the flow within the second throat. This paper briefly describes those methods as implemented into the Wind-US CFD code[3]. CFD simulations were performed prior to the wind tunnel test and the paper discusses the observations on the structure of the shock system and its interactions with the boundary layers. The CFD simulations allowed the exploration of operating the second throat with its throat reduced to its minimum width and at a higher level of back-pressure, which forced the shock system further upstream toward the throat. This manner of operating the second throat is different than the customary manner of operating the second throat. The main observation was that 10x10 SWT could be operated up to Mach 4.0 with the reduced throat width and within the limits of tunnel pressure ratio possible in the 10x10 SWT. The paper discusses the CFD results in support of this observation.

A wind tunnel test was conducted and the procedures for the testing and instrumentation are discussed in the paper. The results of the wind tunnel test are provided for four data points and demonstrate stable operation of the tunnel at Mach 3.5, 3.6, and 3.7. The wind tunnel test stopped at Mach 3.7 due to a hydraulic failure within the tunnel. CFD simulations were performed after the wind tunnel test to validate the CFD methods through comparison to the wind tunnel data. The results of these simulations are discussed within the paper. Unsteady data is presented that show increased dynamic behavior within the second throat. The paper finishes with some conclusions and recommendations for further work.

10X10 FOOT SUPERSONIC WIND TUNNEL

The 10x10 SWT operates between Mach 2.0 and 3.5 and Reynolds numbers per foot between 0.5×10^6 and 2.5×10^6. Figure 1 shows a plan view of the 10x10 SWT. The tunnel is powered by electric drive motors that turn two axial compressors that allow the tunnel to operate continuously in a closed-loop manner (aerodynamic cycle). The tunnel can also be operated in an open-loop manner (propulsion cycle) to allow the testing of propulsion systems involving products of combustion.

The tunnel flow is accelerated to supersonic conditions by a flexible-wall nozzle. Station 0 is the exit of the bellmouth that leads into the flexible-wall nozzle and is labeled in Fig. 1 The walls of the nozzle are remotely-controlled to set the minimum width or throat of the nozzle according to the desired test section Mach number. The flexible-wall nozzle has a rectangular cross-section.

The test section is 40.0 feet long and has a uniform height of 10.0 feet. The sidewalls have a width of 10.0 feet at the start of the test section and gradually increase in width to 10.51 feet at the end of the test section to compensate for boundary layer growth. At Mach 3.5, the height of the boundary layers on the walls are approximately 12 inches. The boundary layer thicknesses are not uniform about the circumference of the test section, but rather have an undulating pattern due to differences in converging-diverging shape of the sidewalls with the flat shape of the ceiling and floor.

Downstream of the test section, the second throat decelerates the supersonic flow to subsonic speeds through a system of shock waves. The second throat has a rectangular cross-section and maintains a constant height of 10.0 feet along its length of 61.0 feet. The second throat is of variable geometry and has sidewalls that consist of moveable, remotely-controlled forward and aft ramps. The forward ramps have a length of 9.67 feet and have leading edges connected to the end of the test section at hinges. The aft ramps have a length of 48.0 feet and have trailing edges connected to the tunnel walls at sliding hinges. The trailing edge of a forward ramp and the leading edge of the corresponding aft ramp are each connected at a hinge. This hinge can be pushed inward to reduce the minimum cross-sectional area of the second throat. The width of this rectangular, minimum cross-sectional area is the second throat width, w_{th}. When the ramps are fully collapsed, the width is w_{th} = 120.0 inches, which makes the second throat approximately a straight, rectangular duct. The second throat was designed for the ramps to be brought fully inward for a minimum width of w_{th} = 66.0 inches, which corresponds to a forward ramp deflection of approximately 13.5 degrees.

Downstream of the second throat, a transition section transitions the rectangular cross-section of the second throat to a circular cross-section with a diameter of 14.14 feet over a length of 33.65 feet. Downstream of the transition section, a subsonic diffusion section with a circular cross-section and a length 92.33 feet leads to station 1 where the diameter is 27.57 feet. Station 1 is labeled in Fig. 1 and is just upstream of Turn 1.

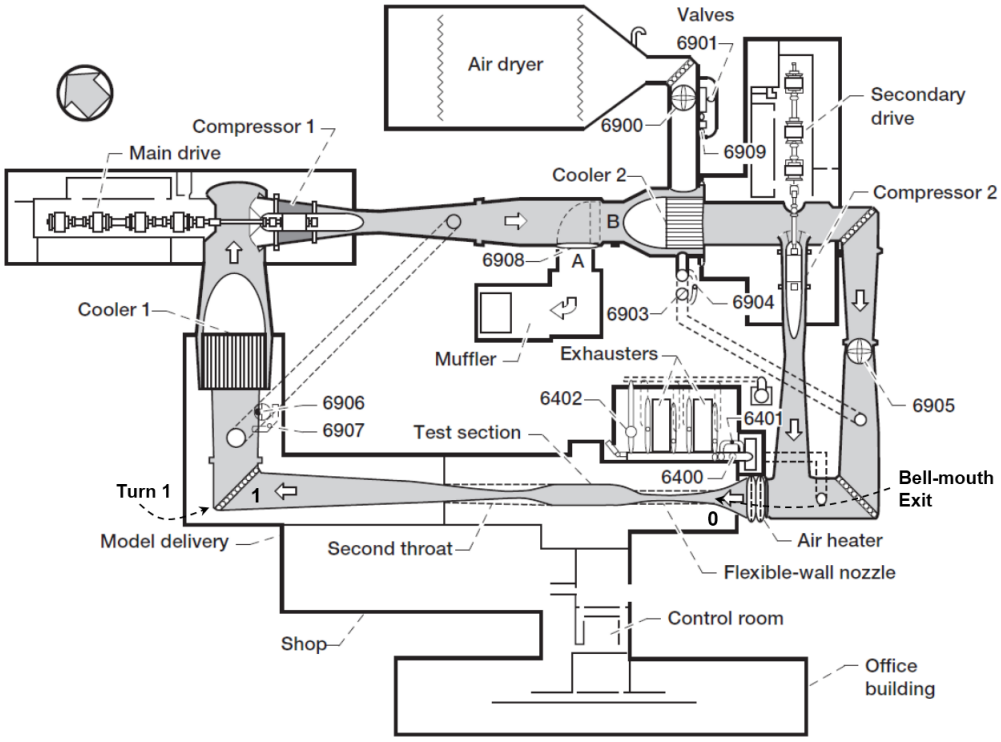

Figure 1. Plan view of the NASA Glenn Abe Silverstein 10x10 foot supersonic wind tunnel.

The compressors provide the total pressure ratio that drives the flow within the tunnel. The total pressure ratio of a single compressor is the ratio of the outlet total pressure to the inlet total pressure. The main compressor has an operating total pressure ratio limit of 2.95. The secondary compressor has an operating total pressure ratio limit of 2.65. The overall compressor pressure ratio is the product of total pressure ratios of each compressor. The overall total pressure ratio required for a particular operating condition depends on the desired test conditions. The secondary compressor can be taken offline if not needed.

The total pressure ratio provided by the compressors has to overcome the losses in total pressure encountered by the flow through the circuit of the tunnel. Most of the losses occur

within the supersonic flow of the test section and the second throat. Within the test section, the flow past the model being tested likely has a combination of shock waves, turbulent boundary layers, and base flows. Within the second throat, the flow is decelerated from supersonic to subsonic through a system of oblique and normal shock waves. In addition, there are shock-wave / turbulent boundary-layer interactions that incur total pressure losses. In other parts of the tunnel circuit, the flow is subsonic and losses are due to viscous drag over the walls of the ducting and past objects within the flow.

The tunnel pressure ratio (TPR) is defined as the ratio of the total pressure at the exit of the bellmouth (station 0) to the total pressure at the entrance to Turn 1 (station 1). Thus,

$$\text{TunnelPressureRatio, TPR} = \frac{p_{t0}}{p_{t1}} \tag{1}$$

For the tunnel to operate, the tunnel pressure ratio has to be below the limiting tunnel pressure ratio, $\text{TPR}_{\text{limit}}$. This limit is determined by the operating limits of the compressors and the losses in the flow as it travels downstream of station 1, through the compressors, and back to station 0. Based on prior measurements, the losses in the tunnel circuit from station 0 to station 1, which is represented by TPR, are estimated to be 10% less than the overall compressor pressure ratio. Thus, the operating limit for the tunnel pressure ratio is computed as

$$\text{TPR}_{\text{limit}} = \frac{(2.95)(2.65)}{(1.10)} = 7.11 \tag{2}$$

This limit is considered to be conservative. The compressors have been operated at higher pressure ratios without compressor stall. Thus, there is potential for the 10x10 SWT to be operated at higher tunnel pressure ratios to overcome increased losses associated with operation at Mach 4.

The tunnel pressure ratio reflects the level of “back-pressure” experienced by the shock system in the second throat. The level of back-pressure is characterized by the ratio of the static pressure in the subsonic flow downstream of the shock system (station 1) to the static pressure at the exit of the bellmouth (station 0), or p_1/p_0. Typically, when tunnel pressure ratio is reduced, the shock system moves upstream along the aft ramps of the second throat. The shock system experiences lower Mach numbers, which decrease the losses through the shock system.

The 10x10 SWT has bypass ducts that allow the compressor flows to bypass the section of the tunnel circuit containing the flexible nozzle, test section, and second throat. These ducts are denoted by dashed lines in Fig. 1. The effect of diverting flow through the bypass ducts is to change the tunnel pressure ratio, which changes the level of back-pressure experienced by the second throat. This procedure was used in the wind tunnel test described below to subject the second throat to varying levels of tunnel pressure ratio and back-pressure.

The ability to operate the 10x10 SWT at test section Mach numbers above 3.5 depends on the ability to maintain a stable shock system within the second throat while keeping total pressure losses within the limits of the tunnel pressure ratio. The approach explored in this study was to reduce the width of the second throat from its nominal width of w_{th} = 98 inches used for current operation at Mach 3.5. This study explored reducing the width toward its minimum of w_{th} = 66 inches. This approach is analogous to increasing the stability of a mixed-compression inlet while increasing efficiency, which translates to reducing total pressure losses. With a decrease in width, the angles of the forward ramps increase, which decrease the Mach numbers downstream of the forward ramp oblique shocks. The increase strength of the oblique shocks does increase the shockwave / boundary layer interactions on the floor and ceiling of the second throat. The effectiveness of this scheme was first explored with CFD simulations of the flow in the second throat.

CFD METHODS

Methods of computational fluid dynamics (CFD) were used to perform computational simulations of the flow through the test section, second throat, and diffuser leading to Turn 1 of

the tunnel. The CFD simulations provided flow properties throughout the flowfield, which allowed greater understanding of the features of the flow in the second throat. The CFD simulation also provided a means for estimating the total pressure losses in the test section and second throat. The ratio of total pressures was compared to the operating limit to evaluate whether or not the compressors could achieve the simulated flow.

Figure 2 shows the portion of the tunnel between the test section and Turn 1 containing the second throat. Also shown is the flow domain used for the CFD simulations. The geometry of the second throat and diffuser leading to Turn 1 were modeled using drawings of the 10x10 SWT. The coordinate system for the flow domain had its origin (x = 0.0) at the end of the test section. The tunnel between stations 0 and 1 had symmetry in its cross-section in both the horizontal and vertical planes. This allowed the flow domain to use of only one-quarter of the tunnel cross-section. Symmetry boundary conditions were imposed at the symmetry flow domain boundaries. The surfaces of the flow domain for the tunnel walls were modeled with adiabatic, no-slip viscous-wall boundary conditions.

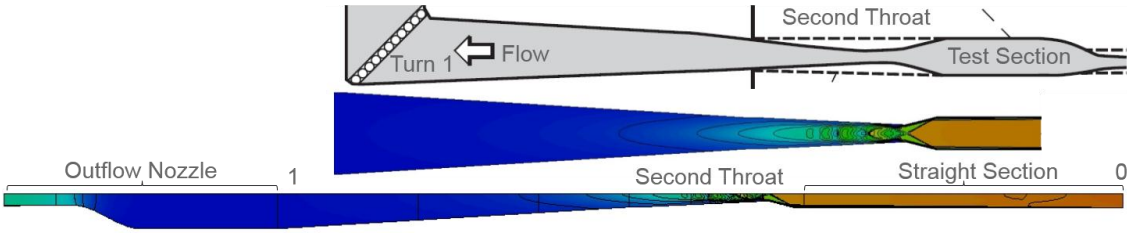

Figure 2. Flow domain for the CFD simulations of the 10x10 SWT second throat.

Upstream of the second throat, the geometry of the test section was modeled with a straight section with a rectangular cross-section having the same dimensions of the cross-section of the end of the 10x10 SWT test section as described in the preceding section. The flexible-wall nozzle was not modeled. Rather, the inflow boundary of the straight section and flow domain was placed about 100 feet upstream of the second throat such as to generate a boundary layer with a uniform thickness of approximately 12 inches about the circumference of the end of the test section. The inflow boundary is labeled in Fig. 2 as station 0 and is analogous to station 0 of Fig. 1. The total pressure and total temperature at station 0 were specified to the expected values at the exit of the bellmouth as presented in Fig. 1. The Mach number at the inflow boundary was specified to be supersonic such that at the end of the test section, the Mach number matched that of the desired supersonic test section Mach number. The supersonic nature of the inflow allowed a fixed-condition boundary condition to be imposed at the inflow.

The flow domain modeled the subsonic diffuser to station 1 as labeled in Figs. 1 and 2. Downstream of the subsonic diffuser, an outflow nozzle was attached to establish the outflow boundary for the flow domain. The outflow nozzle accelerated the subsonic diffuser flow to supersonic conditions at the outflow or end of the nozzle. An extrapolation boundary condition was imposed at the exit of the outflow nozzle. The extrapolation boundary condition reduced the likelihood that the outflow boundary condition would adversely affect the conditions at station 1. The outflow nozzle also provided a means to impose a back-pressure within the diffuser by adjusting the radius of the throat of the outflow nozzle. Decreasing the radius increased the level of back-pressure, reducing the TPR.

The flow domain was discretized using multi-block, structured H-grids. Several grids of varying resolution were used to explore the grid sensitivity of the CFD simulations and to ensure grid convergence. The grid lines were clustered near the walls to resolve the boundary layers on the tunnel surfaces through the viscous sub-layers with a resolution of $y+ \approx 2$ for the first grid point off the wall. In the axial direction, a grid spacing of 2.0 was imposed at the throat of the second throat with a grid spacing of 3.0 inches at the start and end of the ramps. At the horizontal and vertical symmetry planes, a spacing of 2.0 inches was imposed. A condition of grid stretching of 15% was imposed for determining the appropriate number of grid points and distributing the grid points normal to the wall. This resulted in 309 grid points in the axial direction

through the second throat and 85 and 91 grid points in the vertical and cross-flow directions, respectively.

The flow was solved using the Wind-US CFD code[3]. Wind-US solved the Reynolds-Averaged Navier-Stokes (RANS) equations using a cell-vertex, finite-volume representation for which the flow solution was located at the grid points. The temperatures were assumed to be within the limits to allow the use of the ideally-perfect air model. The RANS equations were solved using an implicit time-marching algorithm with a first-order, implicit Euler method using local time-stepping. The flowfield was initialized at all grid points with the supersonic inflow conditions. In Wind-US, local time-stepping was used to converge the flow solution to a steady-state flowfield. All of the simulations reported here assume steady-state conditions. Any small-scale unsteadiness in the flow, such as from shock-wave / boundary layer interactions were damped to provide time-averaged flow properties. The inviscid fluxes of the RANS equations were modeled using a second-order, upwind Roe flux-difference splitting method. The flow was assumed to be turbulent with the turbulent eddy viscosity calculated using the two-equation Menter shear-stress transport (SST) model.

OBSERVATIONS FROM THE CFD SIMULATIONS

The CFD simulations performed prior to the wind tunnel testing provided images of the shock system in the second throat and its interactions with the turbulent boundary layers. In addition, the simulations provided estimates of the total pressure losses through the second throat. This allowed computation of the tunnel pressure ratios, TPR, and determination if the ratios were below the limit established by Eq. 2. CFD simulations were first performed for a test section Mach number of 3.5 to allow comparison with existing calibration data and to explore the effects of reducing the width of the second throat and increasing the back-pressure. CFD simulations were also performed at Mach numbers of 3.6, 3.7, 3.8, 3.9, and 4.0.

The general features of the flow through the second throat can be seen in Fig. 3 for a representative flow solution at Mach 3.5. Figure 3 shows the Mach number contours on the horizontal and vertical symmetry planes of the flow domain within the second throat. The view shows the end of the test section at the lower left. The top surface is the horizontal symmetry plane and shows the outline of the sidewall of the test section and the forward and aft ramps of the second throat. The boundary layers formed on the sidewall ahead of the forward ramp and floor. The forward ramp produced an oblique shock wave which intersected the vertical symmetry plane close to the minimum width of the second throat at the end of the forward ramp. The vertical symmetry plane has the floor of the tunnel along the bottom of the plane. The oblique shock from the forward ramp interacted with the boundary layer on the floor of the tunnel and created a separation bubble. Another oblique shock was formed at the start of the bubble and interacted with the oblique shock from the forward ramp. Downstream of the throat, a shock train was formed through which the supersonic flow decelerated to subsonic flow. The subsonic flow was further decelerated through diffusion in the subsonic diffuser leading to Turn 1.

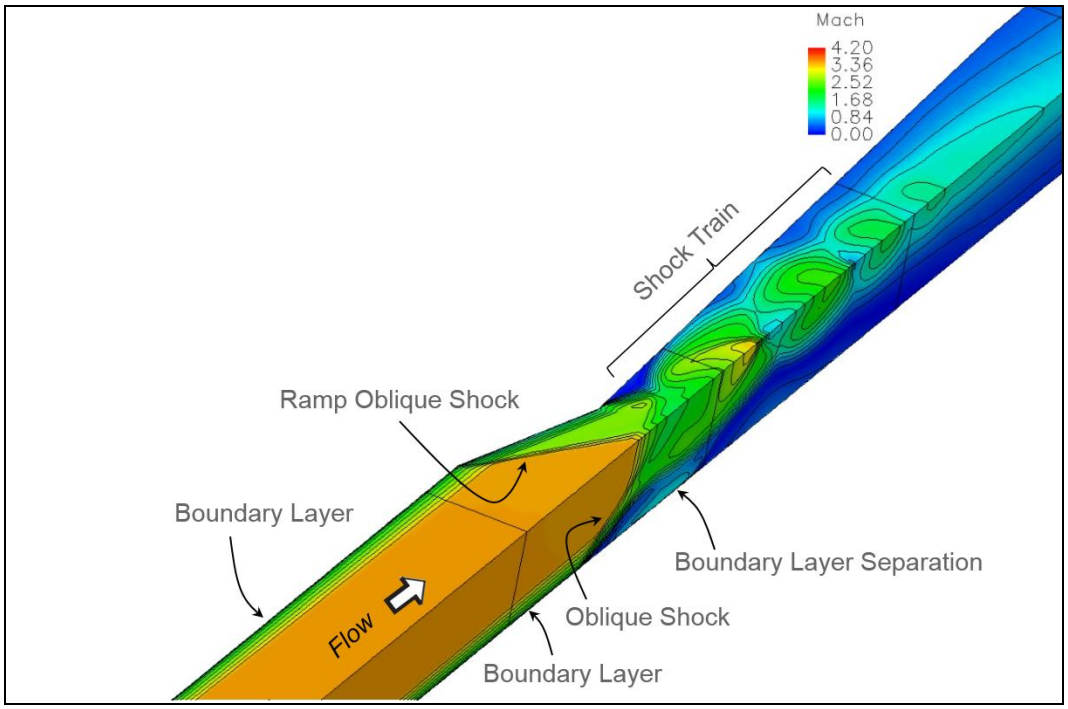

Figure 3. Flow features of the 10x10 SWT second throat.

Table 1 summarizes the conditions and results for some of the CFD simulations performed at Mach 3.5 and 4.0. Some of the simulations were performed prior to the wind tunnel testing and some were performed after using conditions of the wind tunnel test.

Table 1. CFD simulations at Mach 3.5 and Mach 4.0

Mach	w_{th} (in)	p_{t0} (psia)	T_{t0} (°R)	p_1 / p_0	p_{t1} / p_{t0}	TPR
3.50	98.57	33.37	749.51	13.59	0.1475	6.779
				13.92	0.1510	6.621
				(13.82)	*(0.1500)*	*(6.667)*
				14.61	0.1584	6.313
				15.73	0.1703	5.872
				17.04	0.1843	5.426
				17.86	0.1932	5.176
3.50	72.20	25.40	715.22	17.97	0.1943	5.148
				18.49	0.1998	5.004
3.45	98.58	32.93	757.16	12.61	0.1456	6.810
				13.42	0.1549	6.409
3.53	66.00	32.00	760.00	22.50	0.2235	4.475
4.00	66.00	37.00	760.00	23.87	0.1295	7.722
				24.84	0.1348	7.418
				26.22	0.1422	7.032
				27.76	0.1504	6.649

The CFD simulations with a second throat width of w_{th} = 98.57 inches corresponded to nominal operation of the 10x10 SWT at Mach 3.5. The conditions of these simulations correspond to data collected during the wind tunnel testing and comparisons to that data will be presented in a later section. Six levels of back-pressure ranging from p_1/p_0 = 13.59 to 17.86 were established by incremental reductions of the throat of the outflow nozzle. The simulation with a back-pressure of p_1/p_0 = 17.86 was the last stable flowfield before tunnel unstart, which occurred when a higher level of back-pressure was attempted. The simulation with a back-pressure of p_1/p_0 = 13.92 was also performed on a coarse grid to examine the effects of grid resolution on the

flow solution. The coarse grid was obtained by ignoring every other grid point in each of the three coordinate directions of the structured grid. So, instead of 309 axial grid points in the second throat, the simulation used 155 grid points. The resulting pressure ratio, total pressure ratio, and tunnel pressure ratio are listed in Table 1 in parenthesis below the corresponding full grid results. As can be seen, the coarse grid results differed from the full grid results by less than 0.7 percent. This provided confidence that the results on the full grid were grid independent and sufficient grid resolution was used for the CFD simulations.

The resulting total pressure ratio (p_{t1}/p_{t0}) and tunnel pressure ratio (TPR) are listed for each of the simulations in Table 1. The values of total pressure at each of the stations were calculated from the CFD solution through a mass-averaged integration of the flow on the grid plane within the flowfield at the x-coordinates of the respective stations. The calculated tunnel pressure ratio was then compared to the tunnel pressure ratio limit as calculated by Eq. 2. If the calculated total pressure ratio from the CFD simulation was below the tunnel pressure ratio limit, then it was felt that the 10x10 SWT could provide the conditions to realize that flow.

The CFD simulations with a second throat width of w_{th} = 72.20 inches correspond to the alternative operation of the 10x10 SWT at Mach 3.5 with a reduced width to improve the efficiency of the shock system within the second throat. The throat width of w_{th} = 72.20 inches was the minimum that the second throat could be actuated during the testing. Two levels of back-pressure were simulated. The conditions of these simulations also correspond to data collected during the wind tunnel testing.

The results of two other sets of CFD simulations near Mach 3.5 are also listed in Table 1 and were simulations conducted prior to the testing. Also listed in Table 1 are results of CFD simulations conducted prior to testing for Mach 4.0 within the test section. These are listed here for comparison to the results at Mach 3.5.

Figures 4, 5, and 6 show different views of the Mach number contours of the flowfield for several of the simulations of Table 1. The images show the effect of increased back-pressure and reduced second throat width on the flowfield within the second throat. Figure 4 shows the Mach number contours on the horizontal symmetry plane of the tunnel. The computational flow domain only included half of this plane, so the images in Fig. 4 are mirrored about the vertical plane of symmetry to provide a full view of the horizontal cross-section of the flow through the second throat. The flow entered the second throat from the test section at the left of the image. The forward ramps of the second throat created oblique shocks that intersected near the throat. Figure 5 shows the Mach number contours on the vertical symmetry plane. Again, the computational flow domain only included half of this plane, so the images in Fig. 5 are mirrored about the horizontal plane of symmetry. A vertical line was placed in Fig. 5 to indicate the location of the minimum width of the second throat and to provide a reference line for comparison of the Mach contours. Figure 6 shows Mach number contours on axial stations through the second throat for three of the simulations.

Figures 4a and 5a show the contours on the coarse grid corresponding to the Mach 3.5 simulation with the second throat width of w_{th} = 98.57 inches and back-pressure of p_1/p_0 = 13.92. The Mach number contours from the corresponding simulation on the full grid are shown in Figs. 4b and 5b. The contours show essentially the same features, which further provided confidence that the full grid provided sufficient resolution of the flowfields. This flowfield represented the nominal operation of the second throat at Mach 3.5. The shock train consisted of several reflections of shocks at the vertical symmetry plane and at the tunnel sidewalls. The interactions of the shocks with the turbulent boundary layers on the floor and ceiling of the tunnel have limited amounts of boundary layer separation. At about x = 550 inches, the shock approximated a diamond pattern and significant levels of boundary layer separation occurred as the flow became subsonic. The separation regions created oblique shocks in the vertical symmetry plane at the leading edge of the separation bubble. Figure 6a shows attached boundary layers through the throat up to x = 570 inches.

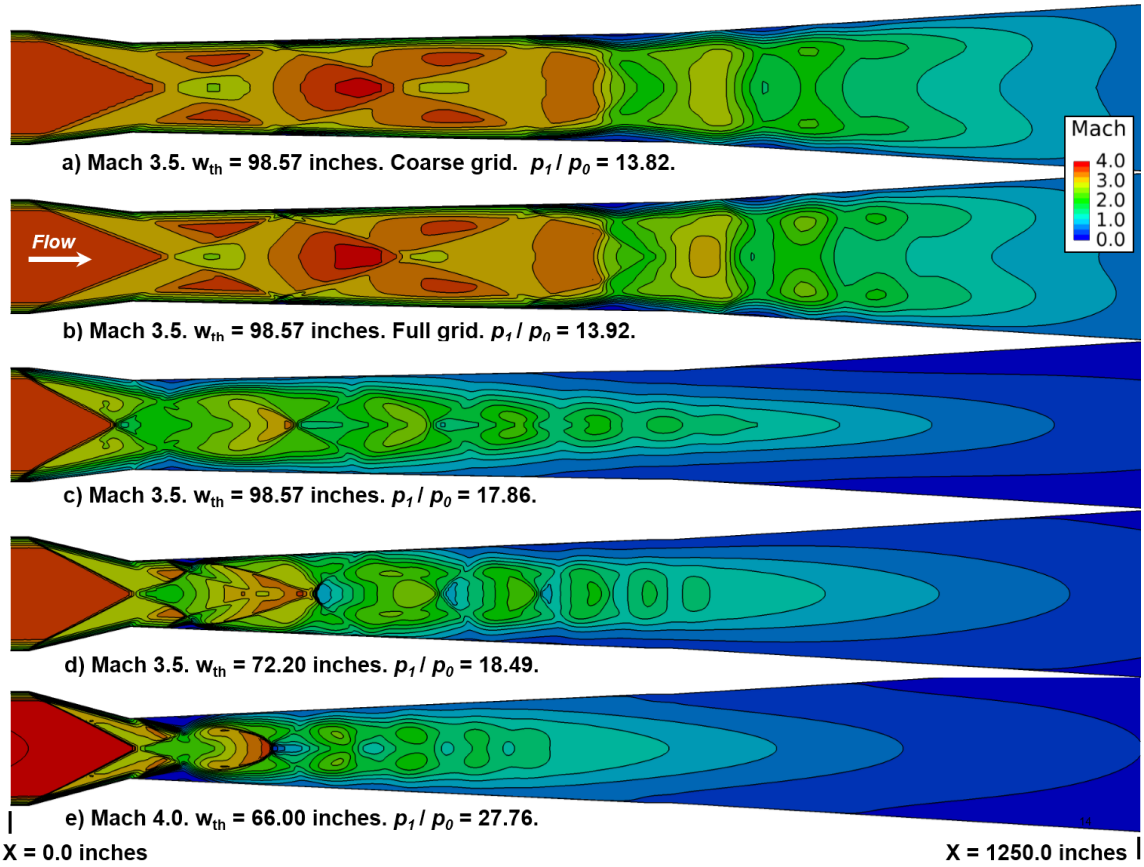

Figure 4. Mach number contours on the horizontal symmetry plane of the 10x10 SWT second throat from the CFD simulations at Mach 3.5 and Mach 4.0.

Figures 4c, 5c, and 6b show the Mach number contours for the Mach 3.5 simulation with the second throat width of w_{th} = 98.57 inches and back-pressure of p_1/p_0 = 17.86. The images show the effect of increased back-pressure without any change in the width of the throat. Table 1 shows that the tunnel pressure ratio reduced from TPR = 6.621 to 5.176 by increasing the back-pressure from p_1/p_0 = 13.92 to 17.86. The reduced total pressure losses likely are due to the lowering of the Mach numbers within the shock system, which reduced the total pressure losses through each shock. The increased back-pressure resulted in boundary layer separation in the corners near the throat. The oblique shocks from the forward ramps had an increased shock angle from the lower back-pressure simulation, which made them stronger and aggravated the shockwave / boundary layer interactions. The separation region in the corner continued along the second throat to downstream of x = 570 inches. While the increased back-pressure helped to reduce losses, the separations are of concern with regards to the unsteadiness and stability of this flow.

The next set of simulations involved reducing the second throat width to w_{th} = 72.20 inches. Figures 4d and 5d show the Mach contours on the horizontal and vertical symmetry planes, respectively, at the reduced throat width with a back-pressure of p_1/p_0 = 18.49. Figure 6c shows the Mach number contours at axial cuts. Table 1 indicates that the tunnel pressure ratio was reduced to a value of TPR = 5.004. The contours of Figs. 4d, 5d, and 6c show that much of the boundary layer separation moved downstream of the throat, as compared to Figs. 4c, 5c, and 6b. This provided confidence that reducing the width of the second throat enhanced the stability of the shock system while improving the efficiency.

Figures 4e and 5e show the Mach number contours on the horizontal and vertical symmetry planes, respectively, when the test section Mach number was increased to Mach 4.0 with a back-pressure of p_1/p_0 = 27.76. The width of the second throat was reduced to the design minimum of

w_{th} = 66.0 inches. The severity of the interactions increased from the Mach 3.5 flowfield; however, many of the same features of the flow were similar between Mach 3.5 and Mach 4.0. The shock system remained stable and the tunnel pressure ratios listed in Table 1 indicated that the TPR was reduced below the tunnel pressure limit as calculated by Eq. 2.

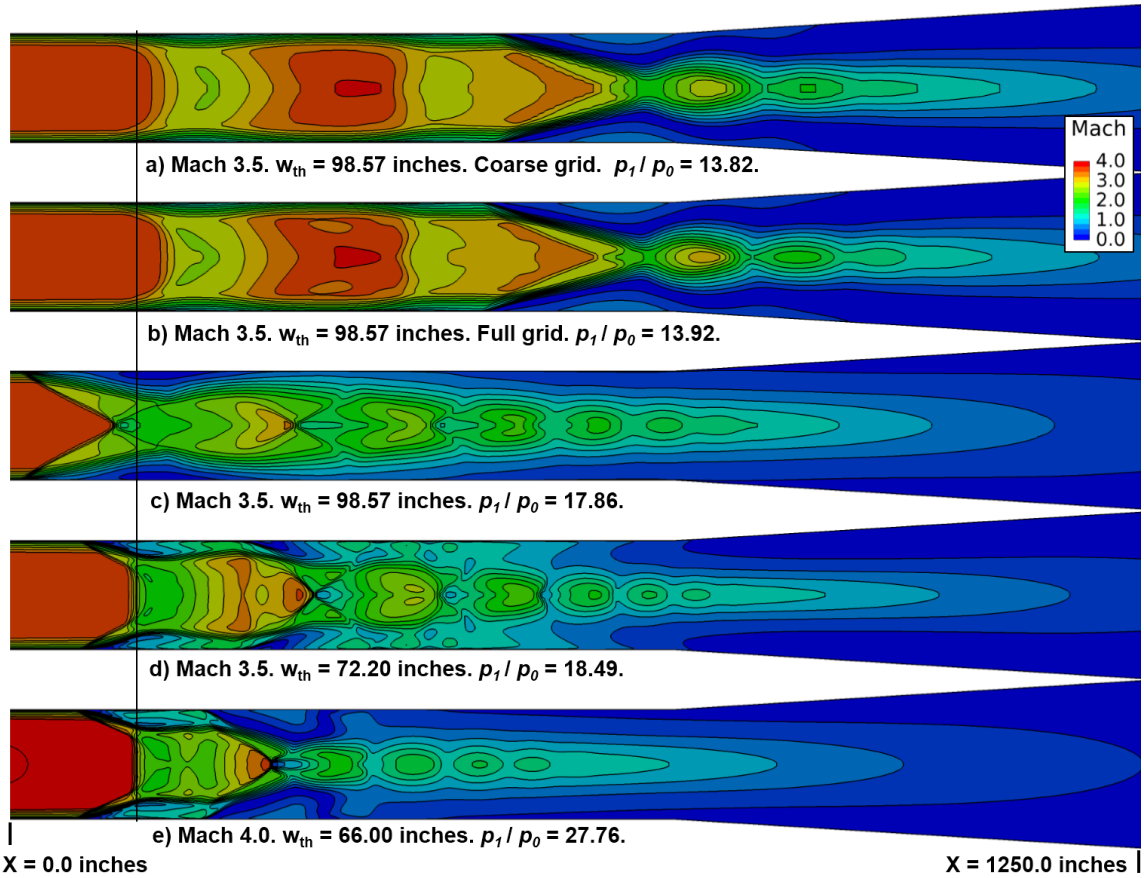

Figure 5. Mach number contours on the vertical symmetry plane of the 10x10 SWT second throat from the CFD simulations at Mach 3.5 and Mach 4.0.

Figure 7 plots the tunnel pressure ratios obtained from the CFD simulations listed in Table 1 along with other CFD simulations at Mach numbers between 3.5 and 4.0. The horizontal line at a tunnel pressure ratio of TPR_{limit} = 7.11 indicates the operating limit on the tunnel pressure ratio as calculated by Eq. 2. The CFD simulations at test section Mach numbers between Mach 3.5 and 4.0 were also performed at a variety of back-pressures. The general trend was that the tunnel pressure ratio decreased with increasing back-pressure. Most simulations at the higher Mach numbers were performed with the width of the second throat closed to its minimum width of w_{th} = 66.0 inches. Some of simulations at Mach 3.5, 3.6, and 3.7 were performed after the wind tunnel test and used conditions of those tests. The data points with open triangular and square symbols correspond to those listed in Table 1 for CFD simulations performed at Mach 3.5 after the wind tunnel testing. The results of Fig. 7 indicate that with the width of the second throat reduced to its minimum width of w_{th} = 66.0 inches, the second throat flow remained started at tunnel pressure ratios below the limit. Therefore, operation of the 10x10 SWT up to Mach 4.0 is possible. The CFD results provided confidence to support a wind tunnel test.

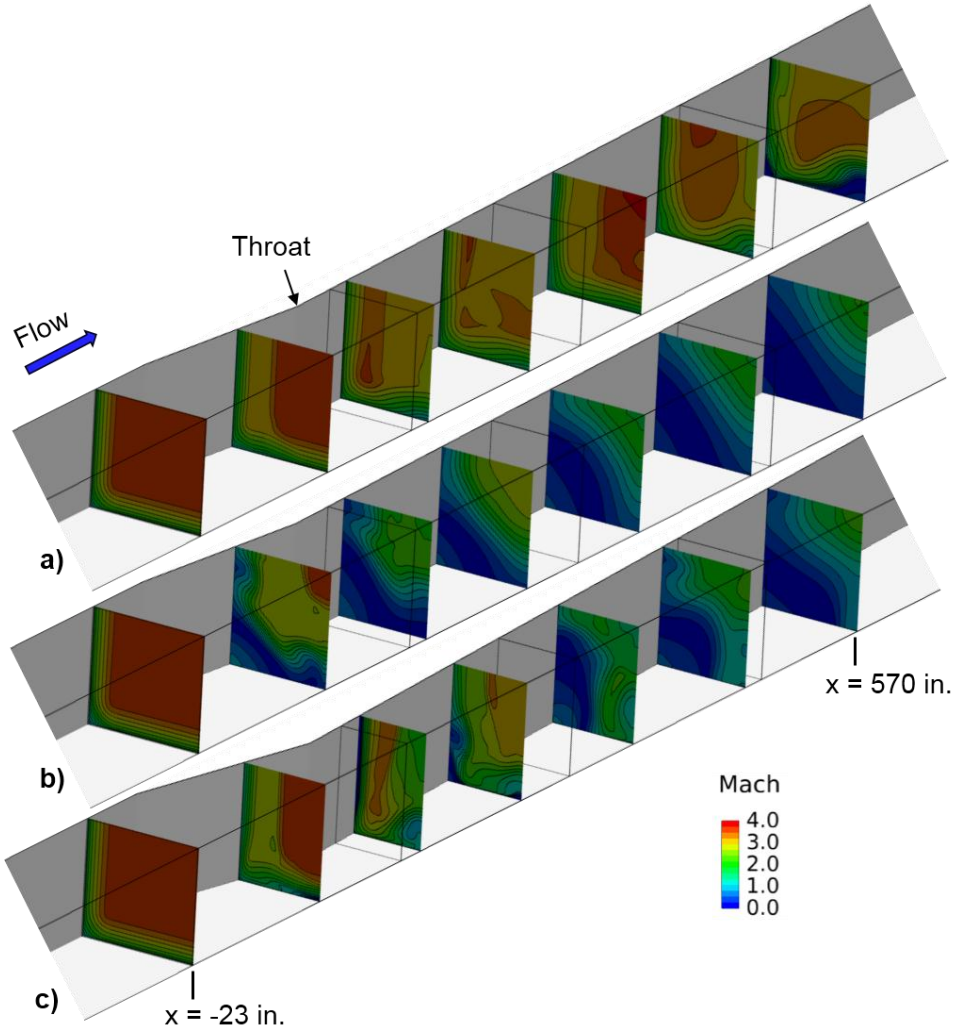

Figure 6. Mach number contours at axial stations of the 10x10 SWT second throat from the CFD simulations at Mach 3.5. a) w_{TH} = 98.57 inches and p_1/p_0 = 13.93, b) w_{TH} = 98.57 inches and p_1/p_0 = 17.86, and c) w_{TH} = 72.29 inches and p_1/p_0 = 18.49.

WIND TUNNEL TEST PROCEDURES

The results of the CFD simulations provided confidence to conduct a wind tunnel test of the 10x10 SWT at increased test section Mach numbers using the strategy of reducing the width of the second throat. The testing was conducted with the tunnel operating in closed-loop mode and without a model in the test section.

The instrumentation of the second throat included numerous static and dynamic pressure ports on the floor, ceiling, and walls. Nine boundary layer rakes were installed to measure the profiles of the boundary layers at various locations. The rakes were selected from existing rakes and ranged in height from 18 to 60 inches. The shorter rakes were placed upstream while the taller rakes were placed downstream where the boundary layer was expected to be thicker and more disturbed due to boundary layer separations and shock interactions. Several of the probes in the rakes contained dynamic pressure transducers to observe the time-varying nature of the pressure. Figure 8 provides diagrams of the top and side views of the second throat showing the general location of the various instrumentation.

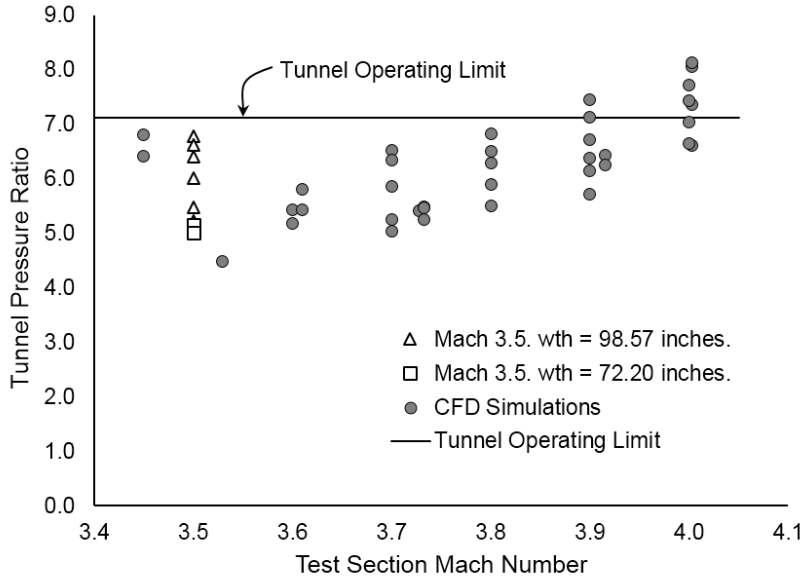

Figure 7. Tunnel pressure ratios from the CFD simulations.

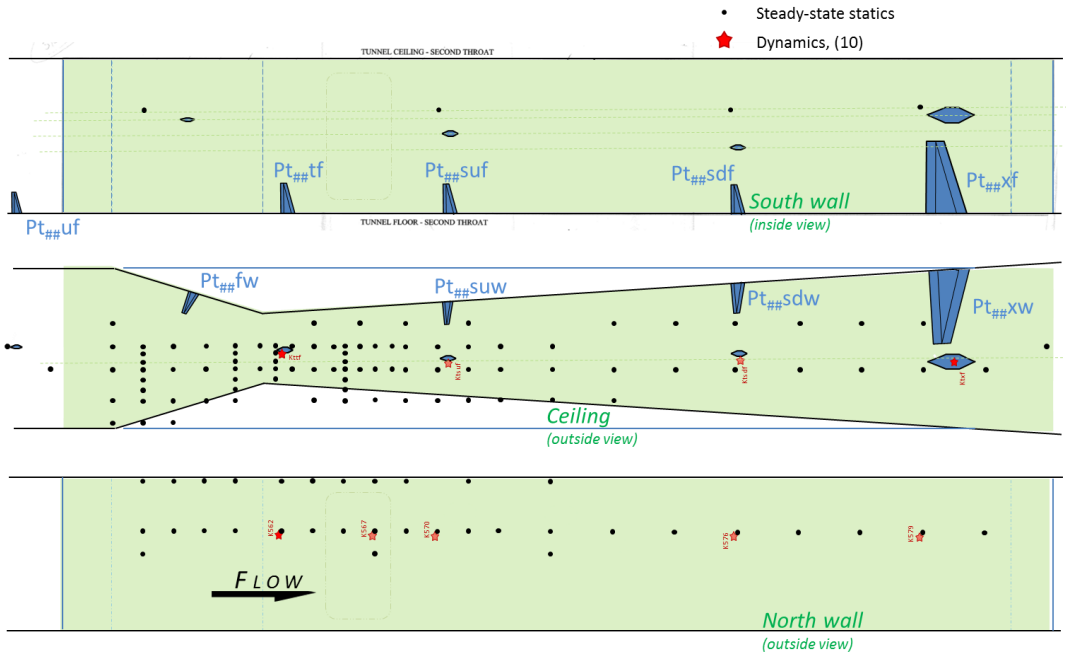

Figure 8. Instrumentation of the second throat for the wind tunnel testing. Steady-state static pressures, dynamic pressure transducer and total pressure rake locations are depicted.

The instrumentation was installed for an initial phase of calibration testing of the tunnel. During this testing, two of the forward 18-inch rakes detached from the floor and traveled downstream into the second throat. It was determined that the rake material at the base attachment was not strong enough to withstand the forces within the 10x10 SWT. Unfortunately, these two rakes were to measure the boundary layer profiles on the floor at the end of the test section and on the forward ramp. These profiles were expected to provide a better understanding of the boundary layer coming into the second throat. One of the rakes hit one of the 60-inch rakes causing damage such that that 60-inch rake had to be removed.

The test plan for the higher Mach numbers involved starting at a test section Mach number of Mach 3.5 and progressing toward Mach 4.0 in steps of Mach 0.1. At each Mach number, the tunnel pressure ratio would be reduced to create an increasing back-pressure for the second throat until the tunnel unstarted. In normal testing, a tunnel unstart would call for a shut-down of the tunnel and inspection of the tunnel and model. However, since there was no model in the test section, it was felt that normal monitoring of the tunnel was sufficient and that the tunnel would not have to be completely shut-down after a tunnel unstart. At Mach 3.5, the width of the second throat was initially set to its nominal width of approximately w_{th} = 98 inches. The width was then reduced to approximately w_{th} = 72 inches, which corresponded to the minimum that could be actuated during the testing. Testing at Mach numbers above 3.5 used a width of the second throat of approximately w_{th} = 72 inches.

The testing was able to collect data at Mach 3.5, 3.6, and 3.7. During the final data collection at Mach 3.7, a serious leak was observed in a hydraulic system of the tunnel and the tunnel was shut down. Upon inspection, it was discovered that a 24-inch rake and the remaining 60-inch rake had detached from the tunnel walls and traveled downstream to the vanes at Turn 1 of the tunnel. It is believed that the unsteady loading and some mounting bolts that lacked sufficient thread engagement contributed to these rake failures.

RESULTS AND DISCUSSION

TUNNEL PRESSURE RATIOS AND STATIC PRESSURES

The validity of the CFD simulations was assessed through comparison of the tunnel pressure ratios and the distributions of the static pressures along the ceiling obtained from the CFD simulations with those obtained from the wind tunnel tests. Table 2 lists data obtained at test section Mach numbers of 3.5, 3.6, and 3.7. Reading 177 represented the nominal second throat width of w_{th} = 98.57 inches for tunnel operation at Mach 3.5. Reading 194 was with the second throat width reduced to w_{th} = 72.20 inches. Some of the results from CFD simulations corresponding to Readings 177 and 194 were presented earlier in Table 1 and Figures 4, 5, and 6. Readings 202 and 210 were at Mach numbers of 3.6 and 3.7 with the second throat width set at w_{th} = 72.54 inches and w_{th} = 71.73 inches, respectively. Table 2 also lists the total pressure, total temperature, and Reynolds number of the flow at the exit of the bellmouth (station 0). The intent was to maintain a constant Reynolds number; however, as the tunnel pressure ratio was reduced through adjustment of the bypass flows around the compressors, the bellmouth total pressure was reduced. Consequently, the Reynolds numbers were was reduced.

Table 2. Wind tunnel test readings used for comparison to CFD simulations.

Reading	Mach	w_{th} (in)	p_{t0} (psia)	T_{t0} (°R)	R_{e0} (/ft)	TPR_{test}	TPR_{CFD}
177	3.5	98.57	33.37	749.51	2.50E+06	7.163	6.621 *(-7.6%)*
194	3.5	72.20	25.40	715.22	2.04E+06	5.323	5.004 *(-6.0%)*
202	3.6	72.54	26.58	724.08	2.09E+06	5.541	5.436 *(-1.9%)*
210	3.7	71.73	31.64	752.29	2.35E+06	6.625	6.339 *(-4.3%)*

Table 2 lists the tunnel pressure ratios observed in the wind tunnel test (TPR_{test}) for each of the readings. The tunnel pressure ratio of Reading 177 is above the limit calculated in Eq. 2; however, the flow within the second throat remained stable. Other data points also had tunnel pressure ratios in excess of TPR_{limit} = 7.11, and also exhibited stable operation of the second

throat. The maximum tunnel pressure ratio observed in the testing was for Mach 3.7 in which $TPR_{test} = 7.64$. Such results provide confidence that the compressor and tunnel could be operated at tunnel pressure ratios in excess of that calculated in Eq. 2.

The tunnel pressure ratio drops from TPR = 7.163 for Reading 177 to TPR = 5.323 for Reading 194. This shows a dramatic increase in efficiency of the second throat by reducing the width of the second throat.

CFD simulations were performed after the wind tunnel testing using the test conditions of each of the Readings as listed in Table 2. For each simulation, the area of the outflow nozzle throat was adjusted until the level of back-pressure (p_1/p_0) closely matched the level of back-pressure recorded for each of the readings of Table 2. The ratio p_{t0}/p_{t1} was computed for each simulation and recorded as TPR_{CFD} in Table 2. The value in the parentheses of the last column of Table 2 is the percent that TPR_{CFD} differed from TPR_{test}. The lower values of TPR_{CFD} suggest that the CFD methods compute lower losses in the second throat than actually occur.

Figure 9 shows the static pressures along the ceiling of the second throat for the readings 177 and 194 for a test section Mach number of 3.5. Also plotted are the static pressure distributions obtained from the CFD simulations. These distributions correspond to CFD simulations listed in Table 1 with back-pressures of $p_1/p_0 = 13.92$ and $p_1/p_0 = 18.49$ for second throat widths of $w_{th} = 98.57$ inches and $w_{th} = 72.20$ inches, respectively. Figures 4, 5, and 6 provided images of those flowfields.

The static pressure distributions of Readings 177 and 194 show similar features. The static pressure reached a local maximum downstream of the intersection of the oblique shocks from the forward ramps at approximately $x = 200$ inches. An expansion occurred and the pressures decreased. As the shock train continued downstream, the static pressures increased along the second throat until they reached a maximum value associated with the level of back-pressure.

In comparing the data of Readings 177 and 194, it can be seen that the smaller throat width of Reading 194 resulted in stronger oblique shocks and greater compression with a higher local maximum downstream of the first intersection of the oblique shocks as compared to that of Reading 177. The local maximum for Reading 194 was slightly upstream of that of Reading 177 due to the higher oblique shock angles of Reading 194. Between $x = 600$ and 900 inches, the static pressure distributions of Readings 177 and 194 indicated a similar, uniform pressure gradient.

The pressure distributions from the CFD simulations followed the trends of the wind tunnel data. The distributions from the CFD simulations tended to yield lower peaks of the local maximum pressures at the intersection of the oblique shocks near $x = 200$ inches. The expansion and recompression of the CFD simulations between $x = 200$ to 400 inches seemed to be well captured. However, between $x = 400$ and 800 inches, the CFD simulation of Reading 177 indicated much lower pressures compared to the data. The pressures of the CFD simulation of Reading 194 showed dramatic oscillation about the data points. Also plotted are the distributions of the static pressures from the CFD simulation computed on the coarse grids. The relatively small differences in the distributions on the coarse and full grids provided further confidence that the CFD solutions were sufficiently resolved on the full grid.

Figure 10 shows the static pressures along the ceiling of the second throat for the Readings 202 and 210 for test section Mach numbers of 3.6 and 3.7, respectively. Also plotted are the static pressure distributions obtained from the CFD simulations. For Mach 3.6, the distributions from two CFD simulations at difference levels of back-pressure are plotted. The distribution for a back-pressure of $p_1/p_0 = 20.08$ approached the pressure at x = 1500 inches; however, the re-compression at $x = 200$ inches was forward of the location indicated by the data. A back-pressure of $p_1/p_0 = 18.79$ put the re-compression in the correct position, but with lower pressures further downstream along the second throat. The static pressure distribution of the CFD simulation at Mach 3.7 matched closely with the data, except between $x = 400$ and 600 inches where oscillations were observed in the pressures of the CFD solution. The cause of this is not clear.

UNSTEADY DATA

The unsteady transducers throughout the tunnel provided data on the time-varying nature of the shock system in the second throat. Figure 11 shows examples of the time histories of the dynamic pressure from several dynamic probes typical of the shock system of the second throat. Fig. 11a shows the pressure responses for nominal second throat operation at Mach 3.5 with the second throat width at w_{th} = 98 inches. For this time history, the pressure recovery was low as the compressors were operating near their maximum pressure ratios. The time duration was only 0.4 seconds and dynamic activity on the wall was significantly downstream of the throat as shown by the DT570 (magenta) pressure trace. Note that low pressure, low noise signals are indicative of steady, supersonic flow. Because the DT570 transducer only intermittently increases from this low pressure base level, the upstream extent of the unsteady shock train had just begun to interact at this location. Interestingly, the adjacent pressure response on the floor rake transducer, DTSUF (gray), shows much more activity. The activity was probably due to the floor boundary layer separation caused by the glancing interaction of the crossing oblique shocks as suggested by the steady-state CFD results of Fig. 3.

When the back-pressure was increased, which reduced the tunnel pressure ratio, increased dynamic activity was found forward of the throat. In Fig. 11b, the increased recovery forced the shock system forward to the minimum throat area as exhibited by the fluctuating pressure on the DT562 transducer (cyan-colored trace). Increased dynamic activity was also observed on nearby downstream transducers, DT567, DT570, and DTSUF. The DTSUF transducer had very high pressure spikes, which suggested that the shock train moved forward of its location. The time history was over a much longer time period of 8 seconds. The irregular buzz cycle suggests frequencies between 1 and 2 hertz. Further review of the dynamic pressure data may provide a diagnostic to ensure safe tunnel operation at higher Mach numbers.

A general observation was that the intensity of the time-varying features of the flow increased when the second throat was closed from the normal width of w_{th} = 98 inches to w_{th} = 72 inches.

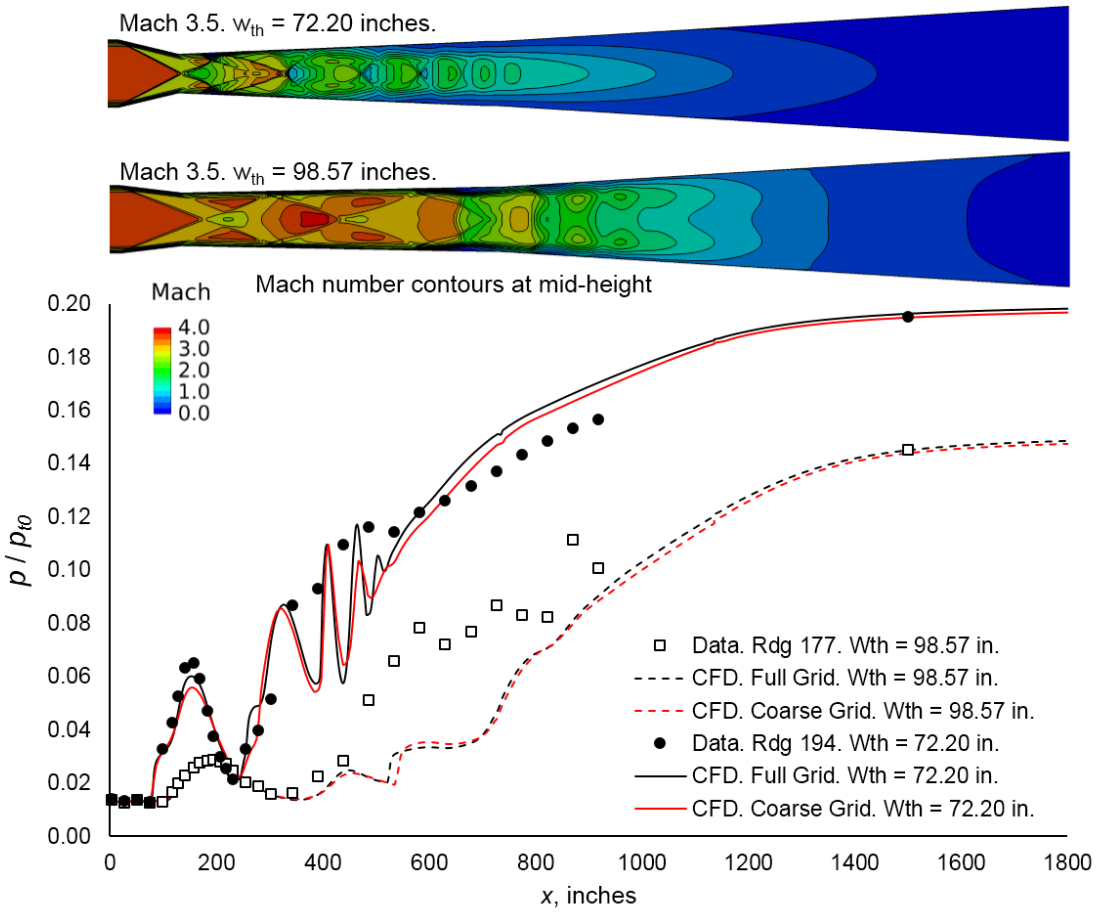

Figure 9. Static pressures along the mid-line of the ceiling for Mach 3.5.

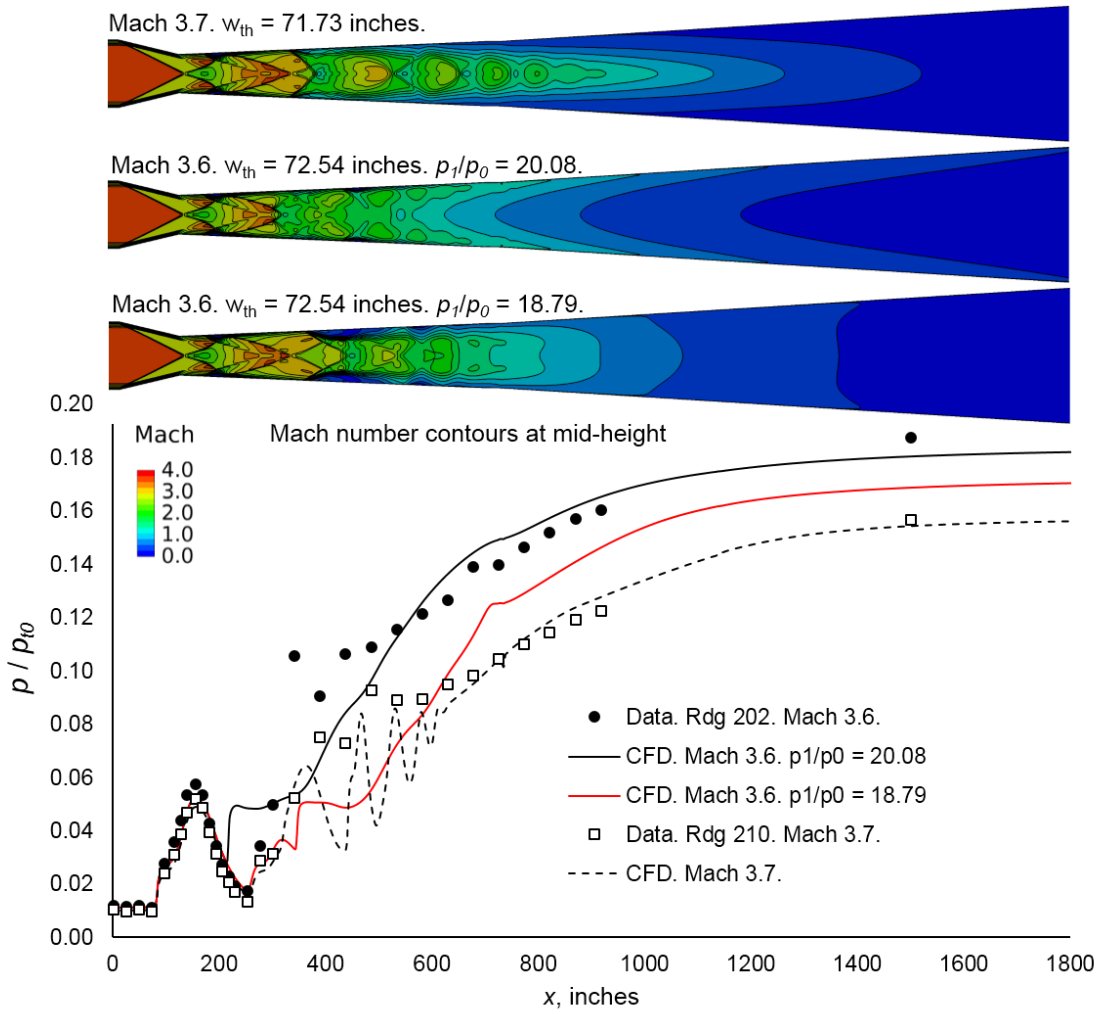

Figure 10. Static pressures along the mid-line of the ceiling for Mach numbers 3.6 and 3.7.

SUMMARY AND CONCLUSIONS

The CFD simulations indicated that operation of the 10x10 SWT up to Mach 4.0 is possible by operating the tunnel with the second throat width reduced to its minimum. The tunnel pressure ratios were below the limit of the compressors. The wind tunnel data show stable operation of the NASA Glenn 10x10 SWT at increased Mach number of Mach 3.6 and 3.7. The results of CFD simulations performed after the wind tunnel test showed reasonable agreement with the test data and provided some confidence of the validity of the CFD simulations. The dynamic pressure data indicated that the unsteadiness of the flow in the second throat increased when the width of the second throat was reduced; however, stable operation was maintained.

FUTURE WORK

There is interest by the authors to continue the exploration of increased Mach number capability for the 10x10 SWT up to Mach 4.0. Obtaining a better understanding of the dynamics of the flow in the second throat is a topic for future work. The CFD analyses need to be expanded to investigate time-accurate simulations to explore the unsteadiness found in the dynamic pressure data. It is reasonable to assume that the shockwave / boundary layer interactions involve an unsteady component not modeled by the current RANS solution methods. CFD simulations could be performed using an approach involving detached-eddy simulation (DES) in which the RANS equations are solved in a time-accurate manner to resolve the boundary layers

while large-eddy simulation (LES) is used to resolve eddies that form in the core flow of the second throat. Another topic of future exploration is the stability of the higher Mach flow in the second throat when a test article is in the test section, which would add blockage and distort the flow entering the second throat.

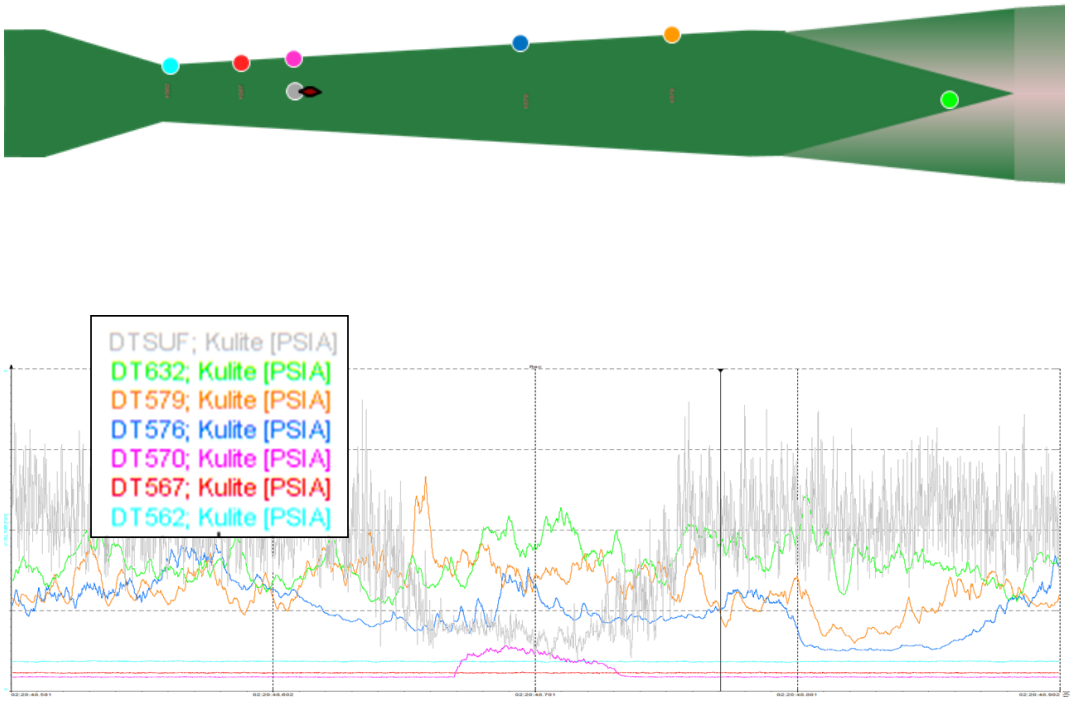

a) Baseline tunnel operation with the shock train downstream. Test section pressure recovery, $P_{t,v1}/P_{t,bm}$ = 0.140. Time duration of 0.4 seconds, all pressures ranged from 0 to 8 psia.

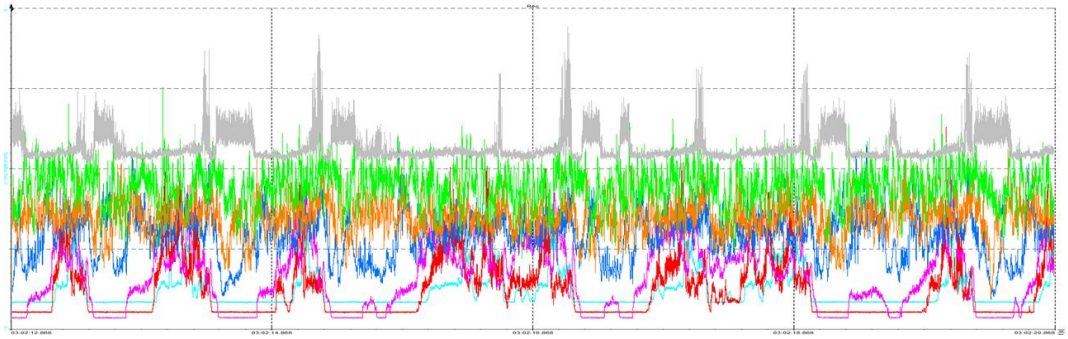

b) Baseline tunnel operation with the shock train upstream. Test section pressure recovery, $P_{t,v1}/P_{t,bm}$ = 0.156. Time duration of 8 seconds, all pressures ranged from 0 to 8 psia, except for DTSUF (-16 to +16 psia).

Figure 11. High-response time histories of dynamic pressures at Mach number of 3.5.

ACKNOWLEDGMENTS

The authors would like to acknowledge the support of the NASA High Speed Project and the Aeronautics Test Program. Key support was provided by the 10x10 SWT personnel throughout the effort as led by Jim Roeder and Julius Giriunas.

REFERENCES

1. Soeder, R. H., Roeder, J. W., Linne, A. A., and Panek, J. W., ***User Manual for NASA Glenn 10- by 10-Foot Supersonic Wind Tunnel***, NASA-TM-2004-212697, NASA Glenn Research Center, Cleveland, OH (May 2004).

2. Liepmann, H.W. and Roshko, A. (1957). "Flow in Ducts and Wind Tunnels". Elements of Gasdynamics. John Wiley.

3. Mani, M., Cary, A., and Ramakrishnan, S., ***A Structured and Hybrid-Unstructured Grid Euler and Navier-Stokes Solver for General Geometry***, AIAA–2004–0524, (January 2004).